INORGANIC CHEMISTRY FRONTIERS

RESEARCH ARTICLE

View Article Online
View Journal | View Issue



Cite this: *Inorg. Chem. Front.*, 2022, **9**, 3771

# Interstitially O-doped $Cd_xZn_{1-x}S$ solid solution derived from chalcogenide molecular clusters for photocatalytic hydrogen evolution†

Weijie Yang, [a,b] Xiang Wang, [b] Zhiqiang Wang,[b] Peipei Sun,[b] Jiaqi Tang,[b] Juan Li,[b] Dong-Sheng Li *[c] and Tao Wu *[a,b]

Received 5th March 2022,
Accepted 25th May 2022

DOI: 10.1039/d2qi00497f

rsc.li/frontiers-inorganic

Interstitial oxygen dopants ($O_i$) in sulfide nanocrystals are more conducive to charge carrier separation for improving the photocatalytic hydrogen evolution (PHE) performance than substituted oxygen dopants ($O_S$). However, oxygen dopants exist dominantly in the form of $O_S$, rather than $O_i$, in oxygen-doped sulfides prepared *via* traditional methods. Herein, an $O_i$-doped $Cd_xZn_{1-x}S$ solid solution was facilely synthesized through pyrolyzing a mixture of oxygen-containing zinc sulfide clusters and $CdCl_2$ salts. At a controlled pyrolysis temperature, the oxygen components inside the cluster were successfully converted into $O_i$ dopants associated with sulfur vacancies. The as-synthesized $O_i$-doped $Cd_xZn_{1-x}S$ solid solution exhibits good PHE performance due to its unique energy band structure caused by the two coexistent defects. The synthetic method of using the intrinsic components in molecular clusters to modulate the types of specific dopants in photocatalysts may provide a new synthetic strategy for creating doped photocatalysts with excellent PHE activities.



## Introduction

Solar water splitting to generate hydrogen over photocatalysts is considered as a promising approach to address the energy crisis and environmental pollution issues.[1–6] Various semiconducting materials, such as metal oxides,[7–9] metal sulfides,[10–16] and carbon nitrides,[17,18] have been investigated as potential candidates for solar water splitting. Among them, metal sulfide solid solutions have attracted the attention of the academic community for a long time because their band gaps can be adjusted in a wide range.[19,20] For example, $Cd_xZn_{1-x}S$ solid solution bears a tunable band gap in the range from 3.6 eV (ZnS) to 2.4 eV (CdS) and exhibits better photocatalytic activity than single ZnS or CdS.[21] Unfortunately, the rapid electron–hole recombination, weak visible light absorption, and poor photocatalytic stability in $Cd_xZn_{1-x}S$ solid solution deteriorated its PHE activity. A simple and common method for solving the above problems is to modify $Cd_xZn_{1-x}S$ by doping with a heterogeneous element, which may narrow the band gap for more light absorption and insert impurity energy levels for better charge separation.[22–25] For example, Chen's group doped $Zn_xCd_{1-x}S$ solid solution with interstitial P element, and the S vacancies associated with the introduction of interstitial P prolonged the lifetime of charge carriers and enhanced the carrier separation efficiency.[24] However, the P atoms with a larger radius relative to S atoms may cause larger lattice distortion of $Zn_xCd_{1-x}S$ solid solution during the doping process and result in the formation of new electron–hole pair recombination centers, which in turn degrade the PHE performance to a certain extent. We believe that introducing interstitial oxygen doping elements with a small atomic radius into $Cd_xZn_{1-x}S$ solid solution is expected to reduce the carrier recombination probability caused by lattice distortion and simultaneously realize rapid photogenerated carrier separation and high PHE performance.

The common synthetic method for doping oxygen in metal sulfide nanocrystals is to add oxygen-containing raw materials during the preparation.[26–28] For instance, Xie's group prepared oxygen-doped $ZnIn_2S_4$ photocatalysts by adding oxygen-containing polyvinyl pyrrolidone during the synthesis, wherein the type of oxygen dopant was substituted oxygen ($O_s$) rather than interstitial oxygen ($O_i$).[28] Unfortunately, such substituted oxygen dopants are inferior to interstitial oxygen dopants in

[a]*College of Chemistry and Materials Science, Guangdong Provincial Key Laboratory of Functional Supramolecular Coordination Materials and Applications, Jinan University, Guangzhou, Guangdong 510632, China. E-mail: wutao@jnu.edu.cn*
[b]*College of Chemistry, Chemical Engineering and Materials Science, Soochow University, Suzhou, Jiangsu 215123, China*
[c]*College of Materials and Chemical Engineering, Hubei Provincial Collaborative Innovation Center for New Energy Microgrid, Key Laboratory of Inorganic Nonmetallic Crystalline and Energy Conversion Materials, China Three Gorges University, Yichang, Hubei 443002, China. E-mail: lidongsheng1@126.com*

† Electronic supplementary information (ESI) available. See DOI: https://doi.org/10.1039/d2qi00497f

promoting carrier separation since interstitial oxygen dopants are often associated with S vacancies. These two different types of defects can trap electrons and holes, respectively, which is better for improving the charge separation efficiency.[24,29] Therefore, to improve the photocatalytic performance of metal sulfides, it is particularly necessary to seek synthetic methods for introducing interstitial oxygen dopants into metal sulfide nanocrystals.

Herein, we intentionally used well-defined oxygen-containing zinc sulfide molecular clusters (denoted as ZSP, Scheme 1a) as the precursor to prepare oxygen-doped metal sulfide semiconductors. The title sample of $Cd_xZn_{1-x}S$ solid solution (denoted as 500-Cd) with abundant S vacancies ($V_S$) and interstitial oxygen ($O_i$) was synthesized by pyrolyzing a mixture of cluster-based crystals and $CdCl_2$ salts at 500 °C under $N_2$ (Schemes 1c and d). Comparative synthesis experiments showed that the temperature control and introduction of $CdCl_2$ salts were key to the conversion of oxygen elements in metal sulfide molecular clusters into $O_i$ (Schemes S1 and 2†). The prepared $O_i$-doped $Cd_xZn_{1-x}S$ photocatalyst (*i.e.*, 500-Cd) exhibited an excellent PHE performance (1240 μmol $h^{-1}$ $g^{-1}$), which is 29.5 and 3.3 times higher than that of ZSP (41 μmol $h^{-1}$ $g^{-1}$) and $Cd_xZn_{1-x}S$ solid solution without $O_i$ dopants (denoted as 400-Cd, 380 μmol $h^{-1}$ $g^{-1}$) in the presence of a sacrificial agent. This is because $O_i$ and $V_s$ introduce new intermediate energy levels, which position near the valence band and between the conduction band and the Fermi level, respectively. Such a band structure may effectively and separately trap holes and electrons to improve the separation efficiency of photogenerated carriers, thereby improving the PHE performance.

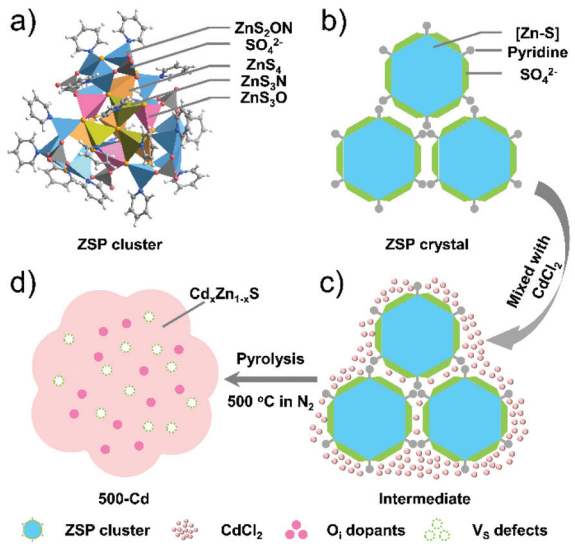


**Scheme 1** Illustration of the fabrication process of $O_i$-doped $Cd_xZn_{1-x}S$ solid solution. (a) Polyhedral model of the [Zn–S–O] molecular cluster. (b) Simplified structure of the ZSP-packed crystal. (c) Simplified model of the mixture of ZSP-packed crystals and $CdCl_2$ salt. (d) $O_i$-doped $Cd_xZn_{1-x}S$ solid solution with the coexistence of $V_s$ defects.

# Results and discussion

## Morphology and structure characterization

The ZSP cluster-based microcrystals were prepared according to a previously reported procedure,[30] and their phase purity was also confirmed through powder XRD measurements (Fig. S1†). The ZSP cluster is a structurally well-defined oxygen-containing zinc sulfide molecular cluster with a formula $[(Zn_{25}S_{19})(SO_4)_6(Py)_{18}]$, which is constructed by a [Zn–S] inner core terminally capped by six sulfate groups and eighteen pyridine ligands. In each ZSP cluster, zinc ions have four types of coordination modes: $ZnS_4$, $ZnS_3N$, $ZnS_3O$, and $ZnS_2NO$ (Scheme 1a). For convenience, the molecular cluster may be simplified as an easily understood structure motif, *i.e.*, the [Zn–S] inner core is wrapped around by sulfate groups and pyridine ligands in the outer layer (Scheme 1b). Such a unique structure was anticipated to be a useful template for constructing an O-doped chalcogenide semiconductor.

To synthesize the $Cd_xZn_{1-x}S$ solid solution, a mixture of ZSP cluster-based microcrystals and $CdCl_2$ powder was pyrolyzed at different temperatures (400 °C, 500 °C, and 600 °C) in $N_2$ for 2 hours (Scheme 1c). The obtained samples are denoted as 400-Cd, 500-Cd, and 600-Cd, respectively (Scheme 1 and S1†). Their structure, composition, and morphology were revealed by TEM and HRTEM images. It was suggested that 400-Cd exists in the form of nanoparticles (NPs) (Scheme S1a† and Fig. 1a), and is identified as $Cd_xZn_{1-x}S$ solid solution due to the clear lattice fringes of 0.33 nm corresponding to the (002) lattice plane of $Cd_xZn_{1-x}S$ (Fig. 1d).[23,31] When the heating temperature was elevated to 500 °C, 500-Cd exhibited a large sheet morphology with a few grain boundaries (Fig. 1b), which is also identified as $Cd_xZn_{1-x}S$ solid solution (Fig. 1e). The elements Cd, Zn, and S were found to be evenly distributed in the solid solution of $Cd_xZn_{1-x}S$ (Fig. S3†). Also, a small amount of oxygen element was present in the $Cd_xZn_{1-x}S$ solid solution. The morphological difference between 400-Cd and 500-Cd may be ascribed to $CdCl_2$.[9,10] In the mixture of ZSP-based microcrystals and $CdCl_2$ salts, $CdCl_2$ wraps around ZSP microcrystals. When the pyrolysis temperature is set at 400 °C, partial $CdCl_2$ salts may diffuse into ZSP microcrystals, and granular $Cd_xZn_{1-x}S$ NPs were gradually formed. Meanwhile, the unreacted $CdCl_2$ salts adsorbed on the surface of NPs may block their further aggregation because $CdCl_2$ is not molten under 400 °C. However, when the pyrolysis temperature is increased above 500 °C, the molten $CdCl_2$ salts combine with the $Cd_xZn_{1-x}S$ NPs, thereby leading to the sheet morphology of 500-Cd and 600-Cd (Fig. 1c). Furthermore, the ZnO phase (PDF#36-1451) is observed in 600-Cd according to the clear lattice fringes of 0.28 nm corresponding to the (100) lattice planes in the HRTEM image (Fig. 1f). These results are consistent with the XRD results (Fig. S2†). Obviously, the oxygen element in ZnO stemmed from the decomposition of $SO_4^{2-}$ anions in ZSP microcrystals. Also, due to the formation of molten $CdCl_2$ salts in 500-Cd and 600-Cd, the oxygen components inside the ZSP molecular clusters were retained during the

 

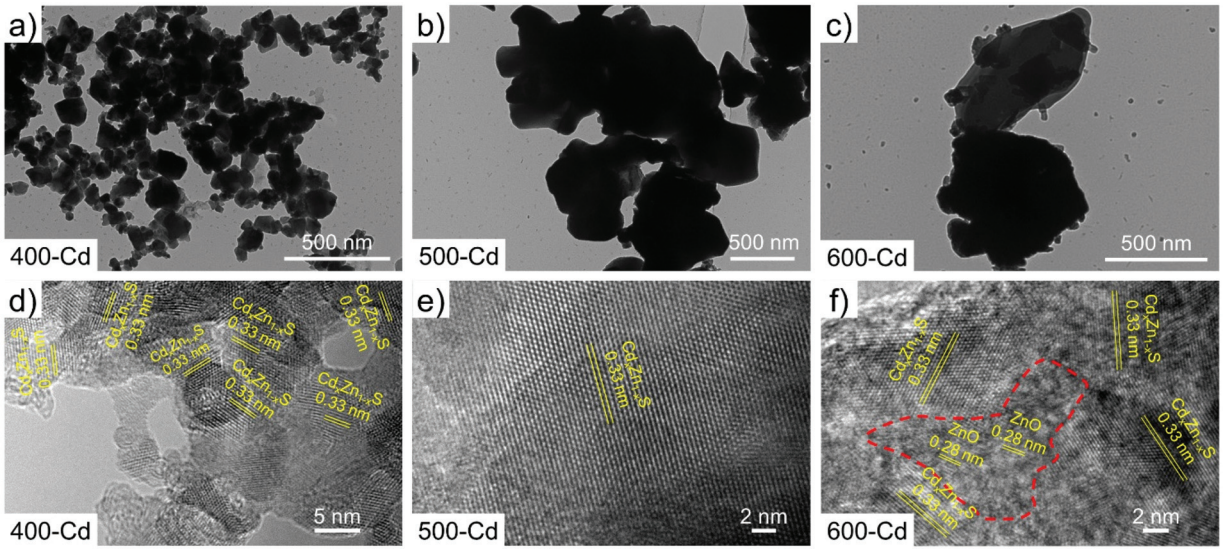


**Fig. 1** TEM images of (a) 400-Cd, (b) 500-Cd, and (c) 600-Cd. HRTEM images of (d) 400-Cd, (e) 500-Cd, and (f) 600-Cd.

pyrolysis of the intermediate mixture to form $Cd_xZn_{1-x}S$ solid solution.

For comparison, pyrolyzed products by directly annealing pure ZSP microcrystals at different temperatures (400 °C, 500 °C, and 600 °C) in $N_2$ were also obtained (Scheme S2†), which are denoted as 400-D, 500-D, and 600-D, respectively. The morphologies of 400-D, 500-D, and 600-D are characterized using TEM and HRTEM images (Fig. S4†). It was clearly observed that 400-D and 500-D were prepared in the form of NPs, and the size of NPs in 400-D is smaller than that of NPs in 500-D (Fig. S4a and b†). The NPs in 600-D present signs of merging (Fig. S4c†). This is caused by the absence of $CdCl_2$ salts. The NPs in 400-D and 500-D are characterized as the ZnS phase because the clear lattice fringes of 0.31 nm corresponding to the (006) lattice planes of ZnS (PDF#89-2739) are observed in the HETEM images (Fig. S4d and e†). These results were consistent with the XRD results (Fig. S5†). In addition, the sample of 600-D contains a partial ZnO phase because the lattice fringes of 0.28 nm corresponding to the (100) lattice planes of ZnO (PDF#36-1451) are observed in the HRTEM images (Fig. S4f†). This phenomenon is similar to that observed in 600-Cd. Considering that the oxygen species are not found in the samples of 400-D, 500-D, 400-Cd and 500-Cd, we can't help but wonder where the oxygen components are at low temperatures (400 °C and 500 °C).

To determine the existing form of the oxygen species in the pyrolyzed samples, X-ray photoelectron spectroscopy (XPS) was conducted on all of the above samples. The XPS scan survey spectra of 400-Cd, 500-Cd, and 600-Cd confirm the presence of Zn, O, Cd, C, and S elements in the as-synthesized samples (Fig. S6†). Fig. S7† shows the high-resolution XPS spectra of C 1s, Cd 3d, Zn 2p, and N 1s. It is clearly observed that the peaks of Cd 3d in 400-Cd, 500-Cd, and 600-Cd shift slightly to lower binding energy (Fig. S7b†). However, the Zn 2p XPS peaks shift first to a lower binding energy, then to a higher binding energy with increasing pyrolysis temperature (Fig. S7c†). This may be attributed to the formation of ZnO at high pyrolysis temperature. Meanwhile, there are no N 1s XPS peaks observed in all samples (Fig. S7d†), suggesting that pyridine molecules are not retained in $Cd_xZn_{1-x}S$ solid solution. In addition, the high-resolution XPS spectra of S 2p and O 1s are also characterized to determine the existing form of O species (Fig. 2a and b). There are two kinds of S 2p XPS peaks, corresponding to $SO_4^{2-}$ and Zn–S bonds, and the weak XPS signals of $SO_4^{2-}$ observed in all samples suggest that $SO_4^{2-}$species are easily pyrolyzed in the presence of $CdCl_2$. As shown in Fig. 2b, 400-Cd exhibits three O 1s XPS peaks at 532.83, 531.99, and 531.29 eV, which are assigned to water, hydroxyl groups, and lattice oxygen, respectively.[26,28] This might be because $SO_4^{2-}$ anions are not pyrolyzed completely under 400 °C. However, a new XPS peak at 530.29 eV is observed in 500-Cd. We conjecture that this peak is attributed to $O_i$, *i.e.* the O anions are doped into the interstitial lattice of $Cd_xZn_{1-x}S$ solid solution. To test our guess, electron spin resonance (ESR) measurements were employed to further confirm the existence of interstitial oxygen dopants in all samples. As shown in Fig. 2c, pristine ZSP microcrystals have no ESR signal. However, 400-Cd shows a clear ESR signal at 327 mT ($g$-value of 2.001), and 500-Cd exhibits two ESR signals at 312 mT ($g$-value of 2.096) and 335 mT ($g$-value of 1.953), respectively. By contrast, a large number of other ESR signals are observed in 600-Cd. According to the literature,[32,33] the EPR signal at $g$ = 2.096 was ascribed to S vacancies. Similarly, we think that the EPR signal at $g$ = 1.953 is attributed to interstitial O ($O_i$) dopants in 500-Cd.[34,35] For further comparison, the existing type of oxygen species in 400-D, 500-D, and 600-D was also analyzed by XPS and ESR measurements (Fig. 2d–f and S8†). Clearly, the high-resolution Zn 2p XPS peaks show the same shift trend as that observed in 400-Cd, 500-Cd, and 600-Cd. According to the N 1s XPS peaks (Fig. S8d†), pyridine molecules are thought to

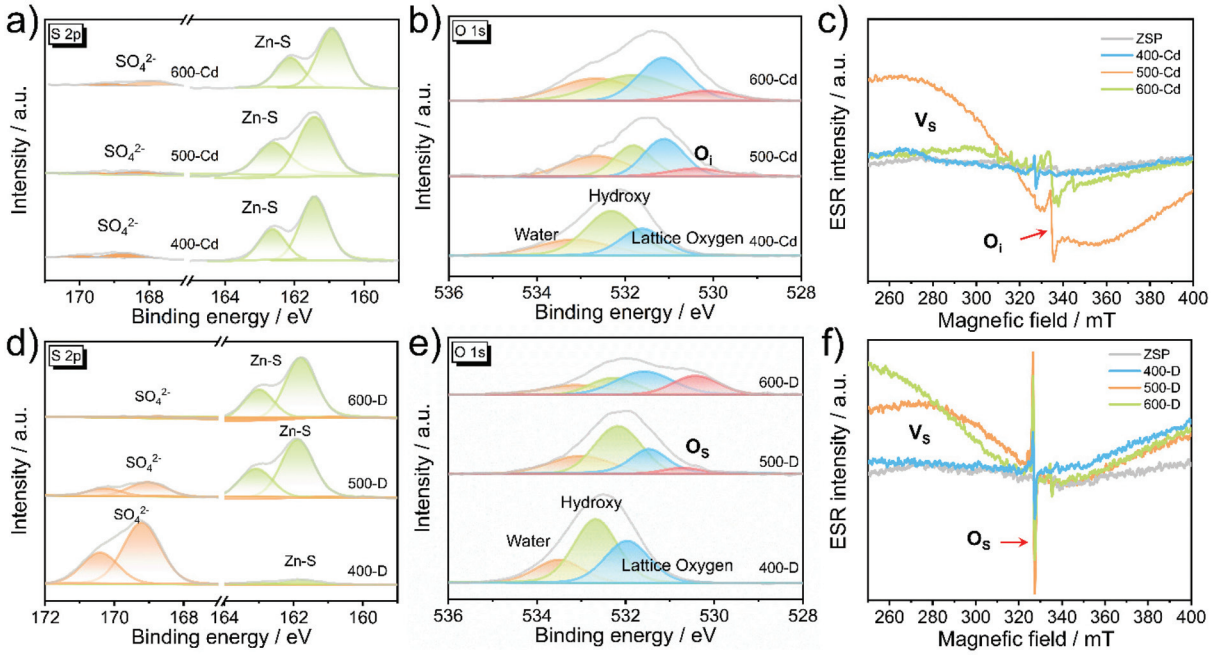


**Fig. 2** High-resolution XPS signals of S 2p (a) and O 1s (b) in 400-Cd, 500-Cd, and 600-Cd. (c) ESR signals of ZSP microcrystals, 400-Cd, 500-Cd, and 600-Cd. High-resolution XPS signals of S 2p (d) and O 1s (e) in 400-D, 500-D, and 600-D. (f) ESR signals of ZSP microcrystals, 400-D, 500-D, and 600-D.

be decomposed, and nitrogen atoms are doped into ZnS (Scheme S1†). $SO_4^{2-}$ anions in pristine ZSP microcrystals are thought to be gradually pyrolyzed into S and O species with the increasing temperature (Fig. 2d). Also, three O 1s XPS peaks in 400-D are assigned to water, hydroxy, and lattice oxygen, respectively (Fig. 2e). In combination with the ESR results (Fig. 2f and Fig. S9†), the new O 1s XPS signal appearing in 500-D and 600-D is assigned to the substituted oxygen ($O_s$). This is because the EPR signal at $g$ = 2.001 in 500-D was significantly different from that in 500-Cd, and, if the interstitial oxygen dopant cannot be formed in 500-D, the oxygen element located in ZnS can only replace the S element to form $O_S$ dopants. Therefore, it was concluded that oxygen species exist in the form of $O_i$ in 500-Cd and 600-Cd, along with the formation of $V_s$, however, in the form of $O_s$ in 500-D and 600-D. Therefore, in the presence of $CdCl_2$ salts, the oxygen components in ZSP are easily converted into interstitial oxygen dopants rather than substituted oxygen dopants.

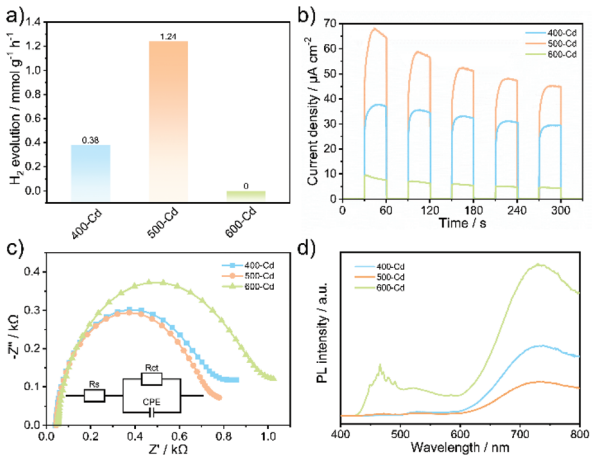


**Fig. 3** (a) The PHE rate, (b) photocurrent response, (c) EIS plots, and (d) PL spectra of 400-Cd, 500-Cd, and 600-Cd.

### Photocatalytic hydrogen evolution performance

PHE experiments were performed under visible-light irradiation using triethanolamine (TEOA) as a hole scavenger. As shown in Fig. S10,† the pristine ZSP microcrystals exhibit a very low PHE activity with a rate of 42 μmol $g^{-1}$ $h^{-1}$, indicating that ZSP is less active for hydrogen evolution. As expected, 500-Cd delivers a high PHE rate of 1.24 mmol $g^{-1}$ $h^{-1}$, which is 29.5 times higher than that of pristine ZSP (Fig. 3a, S10, and S14†). This is ascribed to the formation of the $O_i$-doped $Cd_xZn_{1-x}S$ solid solution. In addition, 500-Cd still exhibits a stable photoactivity after 10 consecutive cycles for a total of 50 h (Fig. S11†). The XRD patterns and TEM images of the cycled samples further confirm the PHE stability (Fig. S12 and S13†). To explain why 500-Cd has higher photocatalytic activity than other samples, photocurrent response experiments were explored. As shown in Fig. 3b, 500-Cd displays the highest photocurrent density, suggesting the fastest photo-generated carrier separation among all samples. Also, according to the results of photoluminescence (PL) and electrochemical impedance spectroscopy (EIS), 500-Cd exhibits the fastest carrier separation efficiency (Fig. 3c and d). For comparison, the PHE performance of 400-D, 500-D, and 600-D samples was also

 

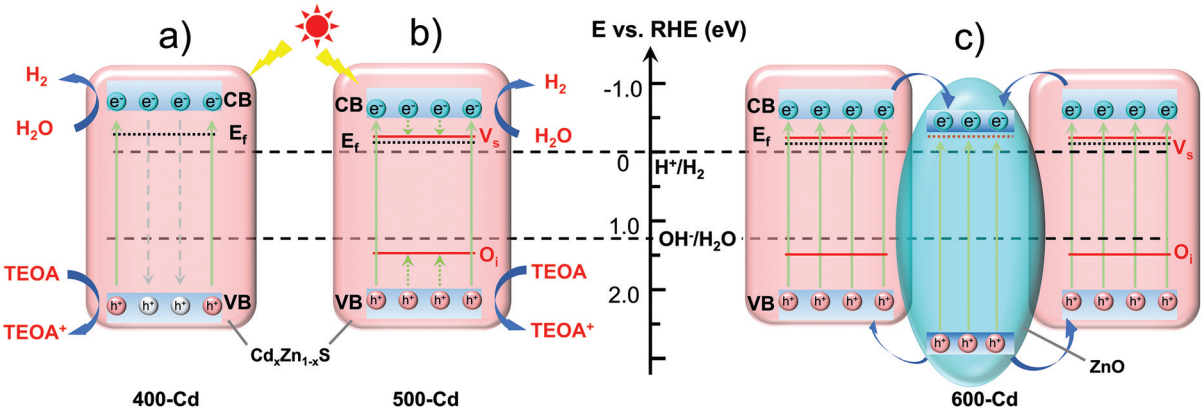


Fig. 4 The diagrams of the energy band structure of 400-Cd (a), 500-Cd (b), and 600-Cd (c).



investigated (Fig. S14†). 500-D delivers a PHE rate of 0.71 mmol $g^{-1}$ $h^{-1}$, which is lower than that of 500-Cd. Also, the results of the photocurrent response, EIS, and PL reveal that the carrier separation efficiency in 500-D is higher than that in both 400-D and 600-D (Fig. S15–S17†), but lower than that in 500-Cd. This could be explained by the different types of oxygen dopants.

### Band structure and photocatalytic mechanism

To understand the PHE mechanism, the energy band structures of photocatalysts are analyzed. As discussed above, the major component in 400-Cd is $Cd_xZn_{1-x}S$ solid solution without any oxygen dopants, 500-Cd consists of $Cd_xZn_{1-x}S$ with $O_i$ dopants and $V_s$ defects, and 600-Cd is the mixture of ZnO and $Cd_xZn_{1-x}S$ with $O_i$ and $V_s$ defects. The band gap ($E_g$) of 400-Cd (2.58 eV) was estimated using the Kubelka–Munk function:[11] $(ah\nu)^2 = A(h\nu - E_g)$ (Fig. S18 and 19†). The valence band (VB) is determined based on the Mulliken electronegativity theory: $E_{VB} = \chi - E^0 + 0.5E_g$, where $E_{VB}$ is the VB edge potential. Moreover, $E^0$ is the energy of free electrons *vs.* NHE (4.5 eV). Finally, $\chi$ is the electronegativity of the semiconductor and is calculated using the following equation:[36] $\chi = [\chi(A)^a\chi(B)^b\chi(C)^c]^{1/(a+b+c)}$, where $a$, $b$, and $c$ are the number of atoms in the compounds. The value of $\chi$ is calculated to be 5.25 eV. Therefore, $E_{CB}$ and $E_{VB}$ of 400-Cd are calculated to be −0.54 and 2.04 eV (*vs.* NHE), respectively. Next, the XPS VB spectra of 400-Cd are analyzed to determine the Fermi level (Fig. S21†).[37] Based on the value of the XPS VB plot (2.24 eV), the Fermi level of 400-Cd is determined to be −0.23 eV (*vs.* NHE), which is close to −0.25 eV using the M–S profile (Fig. S20†). The band energy structure diagram of 400-Cd is shown in Fig. 4a. Similarly, the band gap of 500-Cd is determined to be 2.43 eV. Also, the $E_{CB}$ and $E_{VB}$ of 500-Cd are calculated to be −0.47 and 1.96 eV (*vs.* NHE), respectively. Using the M–S plot in Fig. S20,† the Fermi level is determined to be −0.13 eV (*vs.* NHE).[11,38] It is worth noting that the difference between $E_{VB}$ and $E_f$ is 2.06 eV, while the value of the XPS VB plot of 500-Cd is 1.65 eV (Fig. S22†). This suggests that there is an intermediate level at 1.52 eV between $E_f$ and $E_{VB}$, which may be ascribed to the energy level of $O_i$. Meanwhile, on the basis of previous references, the shallow trap state of $V_s$ locates between the conduction band and the Fermi level at −0.25 eV.[23,29,39] Thus, the band energy structure diagram of 500-Cd is shown in Fig. 4b. This unique energy structure can not only improve the light absorption (Fig. S18†), but also accelerate the photoinduced carrier separation (Fig. 3b–d). This is because the coexistence of $O_i$ and $V_s$ may narrow the band gap to a certain extent. In addition, $O_i$ and $V_s$ are able to separately trap holes and electrons, resulting in fast carrier separation and preventing the recombination of electron–hole pairs. The band structure of 600-Cd is shown in Fig. 4c. The photoexcited electrons in $Cd_xZn_{1-x}S$ solid solution could be transferred to ZnO because ZnO has a more positive conduction band position and more negative Fermi level than $Cd_xZn_{1-x}S$ solid solution, but ZnO locates inside the whole sample (Fig. 1c and f); because $H_2O$ molecules cannot reach the surface of ZnO for the reduction reaction, there is no PHE rate in 600-Cd (Fig. 3a).

## Conclusions

In summary, the $O_i$-doped $Cd_xZn_{1-x}S$ solid solution (500-Cd) with rich S vacancies was fabricated by pyrolyzing a mixture of oxygen-containing chalcogenide microcrystals and $CdCl_2$ salt. The oxygen components in the ZSP cluster were proved to be successfully converted into interstitial oxygen dopants in $Cd_xZn_{1-x}S$ solid solution by controlling the temperature at 500 °C and adding $CdCl_2$ salts. Notably, 500-Cd gives a PHE rate of 1.24 mmol $h^{-1}$ $g^{-1}$, which is 3.3 times higher than that (0.38 mmol $h^{-1}$ $g^{-1}$) of 400-Cd without $O_i$ dopants. Also, the PHE rate of 500-Cd is 1.75 times higher than that (0.71 mmol $h^{-1}$ $g^{-1}$) of 500-D without $O_i$ dopants. The enhanced photocatalytic activity is attributed to the rapid separation of photogenerated electron–hole pairs because the coexistence of $O_i$ dopants and $V_s$ defects allows for trapping holes and electrons separately and simultaneously. Meanwhile, the interstitially O-doped $Cd_xZn_{1-x}S$ solid solution has greater stability than the undoped one during the PHE process. The adopted syn-

thetic method for preparing the $Cd_xZn_{1-x}S$ solid solution with $O_i$ dopants may be a useful synthetic strategy for the creation of specific dopants into photocatalysts for boosting the PHE performance.

## Experimental

### Materials and chemicals

Zinc acetate dihydrate (Zn, 99%, powder), sulfur (S, 99.9%, powder), cadmium chloride ($CdCl_2$, 99%, powder), pyridine (Py, >99%, liquid), 3,5-dimethylpyridine (3,5-DMPy, >99%, liquid), *N*,*N*-dimethylformamide (DMF >99%, liquid), isopropyl alcohol (IPA, >99%, liquid), ethanol (>99%, liquid), and deionized water ($H_2O$, 18.5 MΩ cm) were used as received without further purification.

### Synthesis of ZSP[30]

Zinc acetate dihydrate (60 mg), sulfur (30 mg), pyridine (1.5 mL), and DMF (0.5 mL) were added into a 5 mL glass tube. The vessel was sealed, shaken at room temperature, and then heated at 120 °C for 24 h. The tube was subsequently cooled to room temperature, and then colorless regular rhombic prism crystals were obtained with the yield of 35.0 mg (76% based on the Zn source).

### Synthesis of 400-D, 500-D, and 600-D

A group of samples were synthesized by pyrolyzing the as-synthesized ZSP-based microcrystals in a tube furnace for 2 h under $N_2$ at 400 °C, 500 °C, and 600 °C, respectively. The tube furnace was subsequently cooled to room temperature, and the obtained powders were labeled as 400-D, 500-D, and 600-D, respectively.

### Synthesis of 400-Cd, 500-Cd, and 600-Cd

100 mg of ZSP-based microcrystals and 100 mg of $CdCl_2$ powder were uniformly mixed together. Then, the mixture was heated in a tube furnace for 2 h under a $N_2$ atmosphere at 400 °C, 500 °C, and 600 °C, respectively. After cooling to room temperature, the products were collected, washed several times with $H_2O$ and ethanol, and dried at 60 °C under vacuum. The obtained powders were labeled as 400-Cd, 500-Cd, and 600-Cd, respectively, based on different pyrolysis temperatures.

## Author contributions

Weijie Yang: conceptualization, methodology, investigation, resources, data curation, formal analysis, visualization, and writing – original draft preparation. Xiang Wang: HRTEM characterization of materials, and resources. Zhiqiang Wang: PL characterization of materials and resources. Peipei Sun: UV-vis DRS characterization of materials and resources. Jiaqi Tang: investigation and resources. Juan Li: UV-vis DRS characterization of materials and resources. Dong-Sheng Li: resources, supervision and funding acquisition. Tao Wu: resources, writing – reviewing & editing, supervision, project administration and funding acquisition.

## Conflicts of interest

There are no conflicts to declare.

## Acknowledgements

We acknowledge the financial support from the National Natural Science Foundation of China (No. 21875150 and 22071165) and the 111 Project (D20015).

## Notes and references

1 X. Chen, S. Shen, L. Guo and S. S. Mao, Semiconductor-based photocatalytic hydrogen generation, *Chem. Rev.*, 2010, **110**, 6503–6570.
2 X. Li, J. Yu, J. Low, Y. Fang, J. Xiao and X. Chen, Engineering heterogeneous semiconductors for solar water splitting, *J. Mater. Chem. A*, 2015, **3**, 2485–2534.
3 S. Fang and Y. H. Hu, Recent progress in photocatalysts for overall water splitting, *Int. J. Energy Res.*, 2019, **43**, 1082–1098.
4 Y. Fang, Y. Zheng, T. Fang, Y. Chen, Y. Zhu, Q. Liang, H. Sheng, Z. Li, C. Chen and X. Wang, Photocatalysis: an overview of recent developments and technological advancements, *Sci. China: Chem.*, 2019, **63**, 149–181.
5 Z. Wang, C. Li and K. Domen, Recent developments in heterogeneous photocatalysts for solar-driven overall water splitting, *Chem. Soc. Rev.*, 2019, **48**, 2109–2125.
6 Y. Zhao, S. Zhang, R. Shi, G. I. N. Waterhouse, J. Tang and T. Zhang, Two-dimensional photocatalyst design: A critical review of recent experimental and computational advances, *Mater. Today*, 2020, **34**, 78–91.
7 L. Sun, Y. Zhuang, Y. Yuan, W. Zhan, X. J. Wang, X. Han and Y. Zhao, Nitrogen-Doped Carbon-Coated CuO-$In_2O_3$ p-n Heterojunction for Remarkable Photocatalytic Hydrogen Evolution, *Adv. Energy Mater.*, 2019, **9**, 1902839.
8 C. Zhou, Z. Sanders-Bellis, T. J. Smart, W. Zhang, L. Zhang, Y. Ping and M. Liu, Interstitial Lithium Doping in $BiVO_4$ Thin Film Photoanode for Enhanced Solar Water Splitting Activity, *Chem. Mater.*, 2020, **32**(15), 6401–6409.
9 W. Yang, W. Wu, W. Chen, J. Zhao and X. Hu, Structural modulation of CdS/ZnO nanoheterojunction arrays for full solar water splitting and their related degradation mechanisms, *Catal. Sci. Technol.*, 2018, **8**, 5280–5287.
10 W. Chen, W. Wu, W. Yang, J. Zhao, M. Xiao and W. Kong, $CdCl_2$-assisting heat-treatment: Enhanced photoelectrocatalytic hydrogen generation and stability of CdS/ZnO nanoheterojunction arrays, *Int. J. Hydrogen Energy*, 2018, **43**, 9969–9977.
11 W. Yang, X.-L. Wang, N. Kong, C. Liu, P. Sun, Z. Wang, Y. Ding, H. Lin, D. Li and T. Wu, Minimized external elec-

 

tric field on asymmetric monolayer maximizes charge separation for photocatalysis, *Appl. Catal., B*, 2021, **295**, 120266.

12 D. Liu, Y. Liu, P. Huang, C. Zhu, Z. Kang, J. Shu, M. Chen, X. Zhu, J. Guo, L. Zhuge, *et al.*, Highly tunable heterojunctions from multimetallic sulfide nanoparticles and silver nanowires, *Angew. Chem., Int. Ed.*, 2018, **57**, 5374–5378.

13 Q. Li, X.-Q. Qiao, Y. Jia, D. Hou and D.-S. Li, Amorphous $CoMoS_4$ Nanostructure for Photocatalytic $H_2$ Generation, Nitrophenol Reduction, and Methylene Blue Adsorption, *ACS Appl. Nano Mater.*, 2020, **3**, 68–76.

14 Q. Li, X.-Q. Qiao, Y. Jia, D. Hou and D.-S. Li, Noble-metal-free amorphous $CoMoS_x$ modified CdS core-shell nanowires for dramatically enhanced photocatalytic hydrogen evolution under visible light irradiation, *Appl. Surf. Sci.*, 2019, **498**, 143863.

15 L. Shang, B. Tong, H. Yu, G. I. N. Waterhouse, C. Zhou, Y. Zhao, M. Tahir, L.-Z. Wu, C.-H. Tung and T. Zhang, CdS Nanoparticle-Decorated Cd Nanosheets for Efficient Visible Light-Driven Photocatalytic Hydrogen Evolution, *Adv. Energy Mater.*, 2016, **6**, 1501241.

16 Y. Zhu, X. Jiang, L. Lin, S. Wang and C. Chen, Fabrication of ZnS/CdS Heterojunction by Using Bimetallic MOFs Template for Photocatalytic Hydrogen Generation, *Chem. Res. Chin. Univ.*, 2020, **36**, 1032–1038.

17 H. Luo, Y. Liu, S. D. Dimitrov, L. Steier, S. Guo, X. Li, J. Feng, F. Xie, Y. Fang, A. Sapelkin, *et al.*, Pt single-atoms supported on nitrogen-doped carbon dots for highly efficient photocatalytic hydrogen generation, *J. Mater. Chem. A*, 2020, **8**, 14690–14696.

18 G. Li, Z. Xie, S. Chai, X. Chen and X. Wang, A facile one-step fabrication of holey carbon nitride nanosheets for visible-light-driven hydrogen evolution, *Appl. Catal., B*, 2021, **283**, 119637.

19 D. Huang, M. Wen, C. Zhou, Z. Li, M. Cheng, S. Chen, W. Xue, L. Lei, Y. Yang, W. Xiong, *et al.*, $Zn_xCd_{1-x}S$ based materials for photocatalytic hydrogen evolution, pollutants degradation and carbon dioxide reduction, *Appl. Catal. B: Environ.*, 2020, **267**, 118651.

20 C. Zeng, H. Huang, T. Zhang, F. Dong, Y. Zhang and Y. Hu, Fabrication of Heterogeneous-Phase Solid-Solution Promoting Band Structure and Charge Separation for Enhancing Photocatalytic $CO_2$ Reduction: A Case of $Zn_XCa_{1-X}In_2S_4$, *ACS Appl. Mater. Interfaces*, 2017, **9**, 27773–27783.

21 Q. Li, H. Meng, P. Zhou, Y. Zheng, J. Wang, J. Yu and J. Gong, $Zn_{1-x}Cd_xS$ solid solutions with controlled bandgap and enhanced visible-light photocatalytic $H_2$-production activity, *ACS Catal.*, 2013, **3**, 882–889.

22 Y. Wang, J. Wu, J. Zheng, R. Jiang and R. Xu, $Ni^{2+}$-doped $Zn_xCd_{1-x}S$ photocatalysts from single-source precursors for efficient solar hydrogen production under visible light irradiation, *Catal. Sci. Technol.*, 2012, **2**, 581–588.

23 X. Tang, J. H. Zhao, Y. H. Li, Z. J. Zhou, K. Li, F. T. Liu and Y. Q. Lan, Co-doped $Zn_{1-x}Cd_xS$ nanocrystals from metal-organic framework precursors: porous microstructure and efficient photocatalytic hydrogen evolution, *Dalton Trans.*, 2017, **46**, 10553–10557.

24 H.-F. Ye, R. Shi, X. Yang, W.-F. Fu and Y. Chen, P-doped $Zn_xCd_{1-x}S$ solid solutions as photocatalysts for hydrogen evolution from water splitting coupled with photocatalytic oxidation of 5-hydroxymethylfurfural, *Appl. Catal., B*, 2018, **33**, 70–79.

25 K. Khan, X. Tao, M. Shi, B. Zeng, Z. Feng, C. Li and R. Li, Visible-light-driven photocatalytic hydrogen production on $Cd_{0.5}Zn_{0.5}S$ nanorods with an apparent quantum efficiency exceeding 80%, *Adv. Funct. Mater.*, 2020, **30**, 2003731.

26 B. Pan, Y. Wu, B. Rhimi, J. Qin, Y. Huang, M. Yuan and C. Wang, Oxygen-doping of $ZnIn_2S_4$ nanosheets towards boosted photocatalytic $CO_2$ reduction, *J. Energy Chem.*, 2021, **57**, 1–9.

27 X. Yang, Y. Guo, Y. Lou and J. Chen, O-$MoS_2$/$Mn_{0.5}Cd_{0.5}S$ composites with enhanced activity for visible-light-driven photocatalytic hydrogen evolution, *Catal. Sci. Technol.*, 2020, **10**, 5298–5305.

28 W. Yang, L. Zhang, J. Xie, X. Zhang, Q. Liu, T. Yao, S. Wei, Q. Zhang and Y. Xie, Enhanced photoexcited carrier separation in oxygen-doped $ZnIn_2S_4$ nanosheets for hydrogen evolution, *Angew. Chem., Int. Ed.*, 2016, **55**, 6716–6720.

29 R. Shi, H. F. Ye, F. Liang, Z. Wang, K. Li, Y. Weng, Z. Lin, W. F. Fu, C. M. Che and Y. Chen, Interstitial P-doped CdS with long-lived photogenerated electrons for photocatalytic water splitting without sacrificial agents, *Adv. Mater.*, 2018, **30**, 1705941.

30 C. Xue, J. Zhang, X. Wang, M. Gu, Y. Zhu, D. S. Li, J. Guo, Y. Liu and T. Wu, Light-triggered evolution of molecular clusters toward sub-nanoscale heterojunctions with high interface density, *Chem. Commun.*, 2019, **55**, 8146–8149.

31 F.-Y. Tian, D. Hou, F. Tang, M. Deng, X.-q. Qiao, Q. Zhang, T. Wu and D.-S. Li, Novel $Zn_{0.8}Cd_{0.2}S$@g-$C_3N_4$ core–shell heterojunctions with a twin structure for enhanced visible-light-driven photocatalytic hydrogen generation, *J. Mater. Chem. A*, 2018, **6**, 17086–17094.

32 S. Zhang, X. Liu, C. Liu, S. Luo, L. Wang, T. Cai, Y. Zeng, J. Yuan, W. Dong, Y. Pei, *et al.*, $MoS_2$ quantum dot growth induced by S vacancies in a $ZnIn_2S_4$ monolayer: Atomic-level heterostructure for photocatalytic hydrogen production, *ACS Nano*, 2018, **12**, 751–758.

33 C. Du, Q. Zhang, Z. Lin, B. Yan, C. Xia and G. Yang, Half-unit-cell $ZnIn_2S_4$ monolayer with sulfur vacancies for photocatalytic hydrogen evolution, *Appl. Catal., B*, 2019, **248**, 193–201.

34 P. Gu, X. Wang, T. Li and H. Meng, Investigation of defects in N-doped ZnO powders prepared by a facile solvothermal method and their UV photocatalytic properties, *Mater. Res. Bull.*, 2019, **48**, 4699–4703.

35 X.-H. Zhang, N. Li, J. Wu, Y.-Z. Zheng and X. Tao, Defect-rich O-incorporated 1T-$MoS_2$ nanosheets for remarkably enhanced visible-light photocatalytic $H_2$ evolution over CdS: The impact of enriched defects, *Appl. Catal., B*, 2018, **229**, 227–236.

36 M. Mousavi, A. Habibi-Yangjeh and M. Abitorabi, Fabrication of novel magnetically separable nanocomposites using graphitic carbon nitride, silver phosphate and silver chloride and their applications in photocatalytic removal of different pollutants using visible-light irradiation, *J. Colloid Interface Sci.*, 2016, **480**, 218–231.
37 L. Zhang, J. Ran, S. Z. Qiao and M. Jaroniec, Characterization of semiconductor photocatalysts, *Chem. Soc. Rev.*, 2019, **48**, 5184–5206.
38 J. Lin, Y. Dong, Q. Zhang, D. Hu, N. Li, L. Wang, Y. Liu and T. Wu, Interrupted chalcogenide-based zeolite-analogue semiconductor: atomically precise doping for tunable electro-/photoelectrochemical properties, *Angew. Chem., Int. Ed.*, 2015, **54**, 5103–5107.
39 X. Xu, Y. Zhao, E. J. Sie, Y. Lu, B. Liu, S. A. Ekahana, X. Ju, Q. Jiang, J. Wang and H. Sun, Dynamics of bound exciton complexes in CdS nanobelts, *ACS Nano*, 2011, **5**, 3660–3669.